Ultrasonics Sonochemistry 118 (2025) 107349

Contents lists available at ScienceDirect

Ultrasonics Sonochemistry

journal homepage: www.elsevier.com/locate/ultson

Suppressing the jet formation in a bubble pair excited with an ultrasonic pulse

Dániel Nagy *, Ferenc Hegedűs

Budapest University of Technology and Economics, Faculty of Mechanical Engineering, Department of Hydrodynamic Systems, Muegyetem rakpart 3, Budapest, 1111, Hungary

ARTICLE INFO

Keywords:
Bubble jet
Bubble pair
Multiphase flow
Compressible flow
Sonochemistry
Numerical simulation

ABSTRACT

This study numerically explores the suppression of bubble jet formation in oscillating microbubble pairs under excitation with an ultrasonic pulse, focusing on the conditions that lead to bubble collapse without jetting. Bubble jets (i.e., liquid jets penetrating the bubble) are typically observed in collapsing bubble pairs. However, jet formation can be avoided when the distance between the bubbles is kept within a specific range. We investigate identical-sized bubble pairs aligned along an axis and subjected to a single-cycle ultrasound pulse. Simulations are conducted using the axisymmetric assumption with the ALPACA compressible multiphase flow solver. Our findings revealed that the domain where jet formation is suppressed becomes smaller as the bubble compression increases. This is demonstrated by decreasing the bubble size and the excitation frequency, which allows for greater bubble growth. These results indicate that while jet suppression is feasible for bubble pairs with high compression ratios, it becomes increasingly sensitive to distance.

1. Introduction

Bubbles rarely occur in isolation. Cavitation erosion results from the collapse of millions of bubbles near a surface [1–4]. In a sonochemical reactor, where a liquid is subjected to high-amplitude ultrasound, thousands of microbubbles are generated [5–7]. These bubbles periodically expand and collapse, and during significant collapses, temperatures can reach thousands of kelvins inside the bubbles, potentially initiating chemical reactions [8–12]. Although individual bubbles are extremely small, their collective chemical output can be substantial, making this technology effective in numerous fields [13–17]. However, when bubbles are in close proximity, they can dampen the ultrasound field and lose their spherical shape, which may reduce the overall efficiency [18]. Therefore, understanding the various phenomena related to bubble interactions is crucial for optimizing the chemical output of sonoreactors.

Previous studies have employed simplified models, numerical simulations and experimental measurements to investigate the dynamics of bubble pairs under various conditions [19–26]. Han et al. [27] demonstrated control over the direction of bubble jets in pairs of laser-generated bubbles by manipulating their size, position, and the time delay between their generation. Cui et al. [28] produced bubble pairs using electric discharges and found that closely spaced bubbles produce jets directed towards each other. Similarly, Bremond et al. [29] created hemispherical bubble pairs near a surface and subjected them to high-amplitude acoustic waves. They observed jetting in certain cases and successfully replicated these findings using boundary integral simulations. A related study by Chen et al. [30] investigated the effects of an expanding bubble on a pre-existing bubble in equilibrium, documenting phenomena such as bubble jetting and fragmentation.

Liang et al. [31] created a detailed map of bubble behavior in collapsing bubble pairs of approximately the same size. As a function of dimensionless distance and phase difference of their formation, they identified regions where bubbles coalesce, jet towards each other, or jet away from each other. Chew et al. [32] examined bubbles of different sizes and explored different jet directions as a function of parameters. Similarly, Hopfes et al. [33] observed comparable bubble pair behaviors in gelatin, findings that were later reproduced through numerical simulations by Biller et al. [34]. The main limitation of these studies, from the perspective of sonochemistry, lie in the large bubble radii used (several millimeters), the lack of focus on shape stabilization and in the fact that bubbles were not excited by ultrasound.

From the perspective of sonochemistry, when the goal is to produce chemicals inside a bubble, spherical bubble oscillations are advantageous, and bubble jets should be avoided. Several researchers have demonstrated that collapsing bubble pairs exhibit jets oriented towards each other when they collapse in close proximity [27–29]. This phenomenon will henceforth be referred to as "opposing jets in bubble pairs". In contrast, a single bubble subjected to acoustic excitation produces jets directed towards the pressure gradient as observed by Roselló et at. [35].

* Corresponding author.
E-mail addresses: dnagy@hds.bme.hu (D. Nagy), fhegedus@hds.bme.hu (F. Hegedűs).

https://doi.org/10.1016/j.ultsonch.2025.107349
Received 10 February 2025; Received in revised form 28 March 2025; Accepted 10 April 2025
Available online 26 April 2025

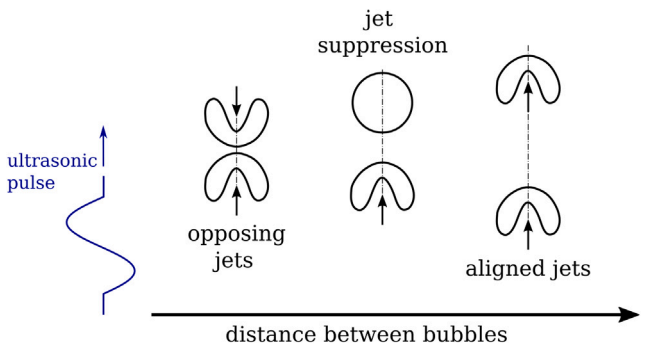

Fig. 1. Jet direction as a function of distance between bubbles in a bubble pair excited by pulsed ultrasound. The ultrasonic impulse propagates upwards. (Image not to scale).

When two bubbles are excited by an ultrasonic pulse, they will jet in the same direction if they are sufficiently far apart since their influence on each other is negligible; this behavior is referred to as "aligned jets in bubble pairs" in this study. Between the domains of opposing and aligned jets, there must exist a transitional region where the jet direction flips. Near this transitional point, conditions may enable a bubble to collapse without jetting. In the rest of this paper, we refer to this behavior as *suppression of jet formation*, or *jet suppression* for short. Jet suppression is qualitatively demonstrated in Fig. 1. The figure qualitatively depicts the expected behavior of bubble pairs excited by an ultrasonic impulse as a function of distance between them. A similar transition was found by Fong et al. [36], Chew et al. [32] and Liang et al. [31] for millimeter sized bubble pairs generated by electric sparks; however, they have not observed jet suppression in measurements nor in numerical simulations. To date, based on our literature review there have been no demonstration of suppression of bubble jets in the transitional region.

The aim of this paper is to demonstrate that the jet suppression of one of the bubbles within a collapsing bubble pair in an acoustic field is achievable through appropriate placement, even if the bubbles themselves are spherically unstable, i.e., the same bubble placed in the acoustic field alone would jet under the same circumstances.

In this study, we use the ALPACA solver [37,38] to simulate two bubbles aligned along an axis and excited by a single ultrasonic pulse (one acoustic cycle). While many experiments utilize acoustic standing waves to study bubble dynamics [39,40], future applications may not necessarily require standing waves. The most significant bubble collapses typically occur within the first few acoustic cycles, and chemical equilibrium is generally reached after only a few such events [41]. Thus, long excitation of the bubbles is not necessary, as beyond the first few collapses, no further useful chemical products are generated. Additionally, bubble jetting often occurs as early as the first collapse [35]. This means that an ultrasonic pulse with only a few cycles may be sufficient for several applications. In this study we also employ an ultrasonic pulse with one cycle.

The paper is structured as follows: In Section 2, the simulation of bubble pairs is introduced, then in Section 3 the phenomena of aligned jets, opposing jets, and jet suppression are investigated. Additionally, convergence studies are presented to verify the accuracy of the simulations, and the results are compared against a coupled spherical bubble model. In Section 4, the domain of jet suppression is discussed, with parameter studies involving 101 different parameter combinations. The findings are then summarized in Section 5.

2. Numerical setup

2.1. Governing equations

The Navier–Stokes equations governing bubble oscillations in compressible liquids read as [37]

$$\frac{\partial \rho}{\partial t} = -\nabla \cdot \rho \boldsymbol{u}, \tag{1}$$

$$\frac{\partial \rho \boldsymbol{u}}{\partial t} = -\nabla \cdot \left(\rho \boldsymbol{u} \otimes \boldsymbol{u} - \Pi\right), \tag{2}$$

$$\frac{\partial \rho E}{\partial t} = -\nabla \cdot \left(\rho E \boldsymbol{u} - \Pi \boldsymbol{u}\right), \tag{3}$$

where ρ is the density, $\boldsymbol{u}$ is the velocity, E is the specific total energy and Π is the stress tensor. In the present study we assume that the effect of heat conduction is negligible, since the bubble collapse is fast. The effect of gravity is also neglected. The stress tensor is

$$\Pi = -p\boldsymbol{I} + \mu\left(\nabla \otimes \boldsymbol{u} + (\nabla \otimes \boldsymbol{u})^{\mathrm{tr}} - \frac{2}{3}\boldsymbol{I}\nabla \cdot \boldsymbol{u}\right), \tag{4}$$

where p is the pressure, μ is the viscosity and $\boldsymbol{I}$ is the identity matrix. Eqs. (1)–(3) are solved in cylindrical coordinate system with axial symmetry for both phases. The interface between the liquid and the gas is tracked by a standard level set method. The following transport equation is solved to track the interface [42]

$$\frac{\partial \phi}{\partial t} + \mathbf{u}_\phi \cdot \nabla \phi = 0, \tag{5}$$

where ϕ is the level set function and $\mathbf{u}_\phi$ is the interface velocity. The level set function gives the signed non-dimensional distance from the interface. The interface is given by $\phi = 0$, and a value of $|\phi| = 1$ means that the point is one cell size away from the interface. Positive signs are assigned to the first phase, while negative signs represent the second phase. To preserve the non-dimensional distance property of the level set, level set reinitialization is employed in every time step [43,44]. Additionally, a cutoff is applied in cells that are located farther away from the interface, limiting the absolute value to $|\phi| = 8$ and preventing far-field fluctuations of the level set.

2.2. ALPACA multiphase flow solver

Throughout this paper, the ALPACA compressible multiphase flow solver is employed, to solve Eqs. (1)–(3). ALPACA utilizes a level set method that solves Eq. (5) for interface capturing and an adaptive multiresolution algorithm for automatic meshing [38,45]. High-order numerical schemes with low dissipation are incorporated to accurately capture shocks [46–48]. Detailed information about the ALPACA solver can be found in its original software publication by Hoppe et al. [37], they have also validated the code with measurements for shock induced bubble jetting. Furthermore, Bußmann et al. [49] validated the ALPACA code for bubble jetting near solid surfaces. Biller et al. [34] have also used ALPACA to study bubble pairs excited by shocks, while Fan et al. [50] employed ALPACA to simulate laser-generated bubble pairs.

In our study, the axisymmetric model is used to mitigate computational costs, limiting the current study to a row of bubbles. As long as bubbles experience excitation along a single axis, the resulting oscillations are axisymmetric [51]; thus, an axisymmetric model can provide meaningful results. In the upcoming bubble pair simulations, only a single ultrasonic pulse is used. Fig. 2 illustrates the simulation setup, featuring two bubbles of the same size situated within a domain of length $l = 2\lambda$ and width $b = \lambda/4$, where $\lambda = c/f$ is the wavelength of the ultrasound, $c = 1496\,\mathrm{m/s}$ is the speed of sound in water in the far field, and f is the excitation frequency. These settings make the simulation domain size significantly larger than the bubble size in each direction.

The bubbles contain ideal gas and are surrounded with water. The bubbles are initially in equilibrium; that is, the initial radius R_0 is the same as the equilibrium radius R_E. The distance between the centers of the bubbles is referred to as D. The center of the bottom bubble is precisely located at $y = \lambda + R_E$; thus, the ultrasonic pulse reaches it at $t = 0$. The dimensionless distance between the bubbles is given according to the literature as follows [23,27,29]:

$$D^* = \frac{D}{R_{\mathrm{top,max}} + R_{\mathrm{bot,max}}}, \tag{6}$$

where $R_{\mathrm{top,max}}$ and $R_{\mathrm{bot,max}}$ are the maximum diameter of the top and bottom bubbles during the expansion, respectively. The maximum

radii are not known in advance; consequently, the D^* values are calculated after the simulations. The gas inside both bubbles is initialized according to the equilibrium condition,

$$p_b = p_0 + \frac{2\sigma}{R_E}, \tag{7}$$

where p_b is the pressure inside the bubble and σ is the surface tension coefficient. The initial velocities are zero and the density is set according to the ideal gas law inside the bubble. The initial conditions in the water in the upper half of the domain (see Fig. 2) correspond to ambient water with density $\rho_0 = 1000\,\mathrm{kg/m^3}$ and pressure $p_0 = 100\,\mathrm{kPa}$. The acoustic impulse is introduced through the initial conditions in the lower half of the domain as,

$$p(x,y) = p_0 + p_A \sin(ky), \tag{8}$$

$$u(x,y) = 0, \tag{9}$$

$$v(x,y) = \frac{p_A}{c\rho_0} \sin(ky) \quad \text{and} \tag{10}$$

$$\rho(x,y) = \rho_0 + \frac{p_A}{c^2} \sin(ky), \tag{11}$$

where $c = 1496\,\mathrm{m/s}$ is the speed of sound, p_A is the pressure amplitude and $k = 2\pi/\lambda$ is the wave number. The initial pressure in the simulation is also illustrated in Fig. 2. As the ultrasonic impulse travels upwards, the bubbles first expand during the low pressure part ($p < p_0$) of the wave, then the bubbles collapse during the high pressure part ($p > p_0$). The boundary conditions are applied as follows: a symmetry boundary condition on the west, and zero-gradient type boundary conditions on all other sides. The viscosity of water is $\mu = 1 \times 10^{-3}\,\mathrm{Pa\,s}$, while the viscosity of the gas inside the bubble was neglected. The surface tension coefficient between the phases is $\sigma = 0.0728\,\mathrm{N/m}$.

To close the governing equations in Eqs. (1)–(3) the stiffened gas equation of state (EoS) is employed: [52],

$$p = (\gamma - 1)\rho e - P_\infty, \tag{12}$$

where e is the internal energy and γ, P_∞ are the parameters. In the gas phase, $P_{\infty,g} = 0$; thus, the stiffened gas EoS results in the ideal gas law, with $\gamma_g = 1.4$ being the ratio of specific heats. The water is modeled using $\gamma_l = 4.4$ and $P_{\infty,l} = 6 \times 10^8\,\mathrm{Pa}$ based on Kaiser et al. [53].

The control parameters in this study are the excitation frequency f, the pressure amplitude p_A, the equilibrium bubble radius R_E, and the distance between bubbles D. All other parameters are kept constant or calculated according to the formulas given above.

3. Classification of bubble jets

In this section, the three main phenomena that occurs in bubble pairs excited by ultrasound are introduced:

1. Opposing jets, that occur in case of bubbles in proximity.
2. Aligned jets, where the jet direction aligns with the direction of propagation of the ultrasound pulse.
3. Jet suppression that occurs in the specific small range that separates aligned and opposing jets.

These three jet types are depicted in Fig. 1. Simulation results are also verified with convergence studies in this section for all three jet types, and the spherical dynamics is compared against the coupled Keller-Miksis equation.

3.1. Opposing jets

Opposing jets occur in case of bubbles in close proximity, an example is demonstrated in Fig. 3. During the expansion phase, a flattening of the facing surfaces occur as seen in the first snapshot at 7.04 µs. This flattening is a well-known phenomenon that is observed when bubbles collide and can also be extended to expanding bubbles in ultrasonic field [54]. Flattening occurs when the liquid inertia is greater than the capillary pressure caused by surface tension.

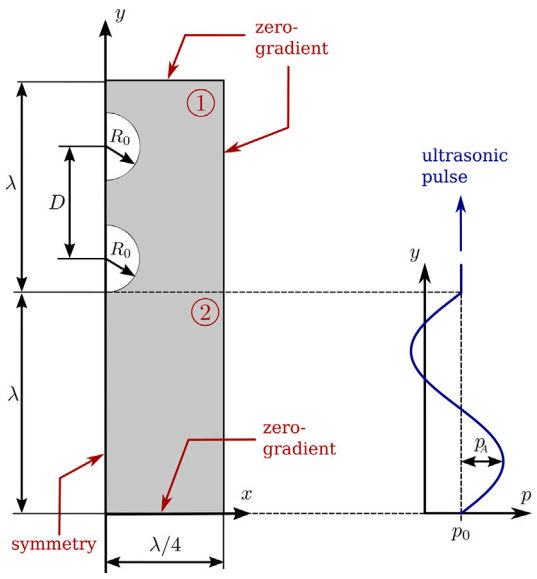

Fig. 2. Boundary and initial conditions for the axisymmetric domain. The control parameters are initial bubble radii $R_0 = R_E$, the distance between the bubble centers D, the acoustic pressure amplitude p_A and the excitation frequency f. The speed of sound is $c = 1496\,\mathrm{m/s}$, the wavelength is $\lambda = c/f$ and the ambient pressure is $p_0 = 100\,\mathrm{kPa}$. The boundary conditions and the initial pressure are also depicted. The figure is not to scale, as $\lambda \gg R_0$.

The bubbles shield the acoustic field; thus, during the collapse, when the surrounding pressure is increasing, the pressure between the bubbles stay consistently smaller. For example, at 10.65 µs, the pressure between the bubbles is 220 kPa, while the pressure above the top bubble and the below the bottom bubble is approximately 270 kPa. The asymmetric bubble shape due to flattening, and the pressure difference across the bubbles result in liquid jets penetrating both bubbles during collapse as observed at 11.55 µs. The jet velocities reach approximately 120 m/s in both bubble jets, and these liquid jets then collide between the two bubbles creating extremely large pressure for a short period of time. The pressure at the colliding jets reach 4100 kPa, while the pressure in the collapsed bubble is only 1800 kPa.

Bubble jets oriented in opposite directions were previously observed also for laser generated bubble pairs near each other [23,27,30], millimeter sized bubble pairs generated by sparks [31,32,36] and for microbubbles with continuous acoustic excitation [55].

3.2. Aligned jets

If a single bubble is placed in the way of an ultrasonic pulse, it may jet during the first expansion-collapse cycle [35]. In such cases, the jet direction aligns with the propagation direction of the impulse. When two bubbles are placed far enough apart, their mutual influence is reduced, and the jet directions in both bubbles remain aligned with the direction of the traveling ultrasonic wave. This phenomenon is illustrated in Fig. 4 for a selected case, where both bubbles exhibit the same jet directions.

Although the bubble expansion and collapse appear nearly spherical, a pressure difference still exists across the bubble due to the nature of the setup, with the ultrasonic pulse propagating upward. This pressure difference arises from the shielding effect of the bubble, where the pressure above the bubble is consistently lower. The pressure difference reaches 5.1 kPa and 1.5 kPa across the bottom and top bubbles, respectively. The pressure difference as a function of time is illustrated in the Appendix in Fig. B.16 for both bubbles. Consequently, the center

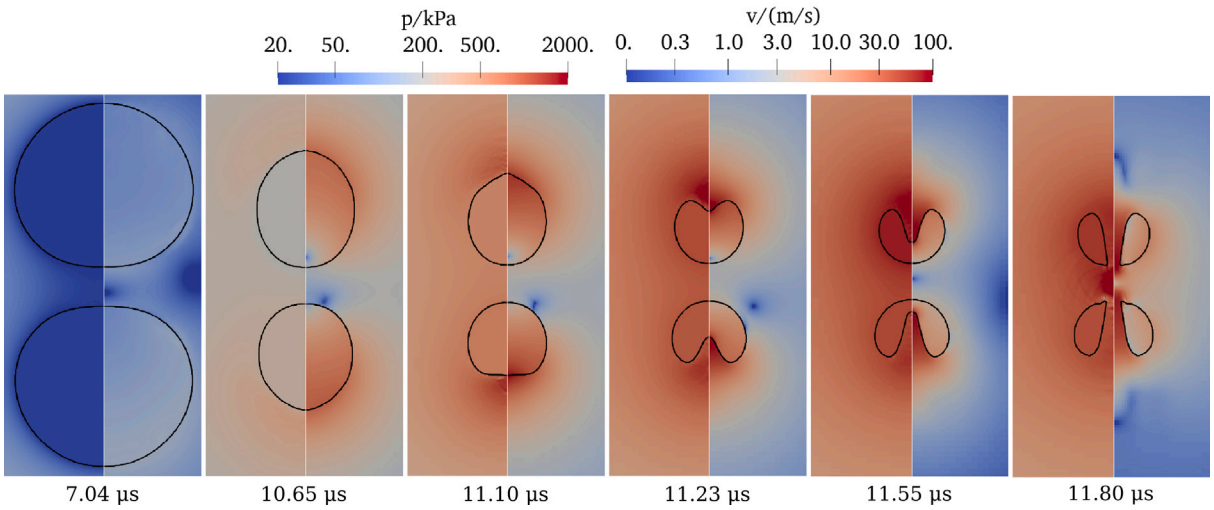

Fig. 3. Opposing jets in the case of two bubbles placed in a distance $D^* = 1.039$, with equilibrium bubble radii $R_E = 40\,\mu m$. The bubbles are excited with a single ultrasonic pulse with frequency $f = 100\,kHz$ and amplitude $p_A = 150\,kPa$. The left and right side of each snapshot is colored according to the pressure and velocity magnitude, respectively.

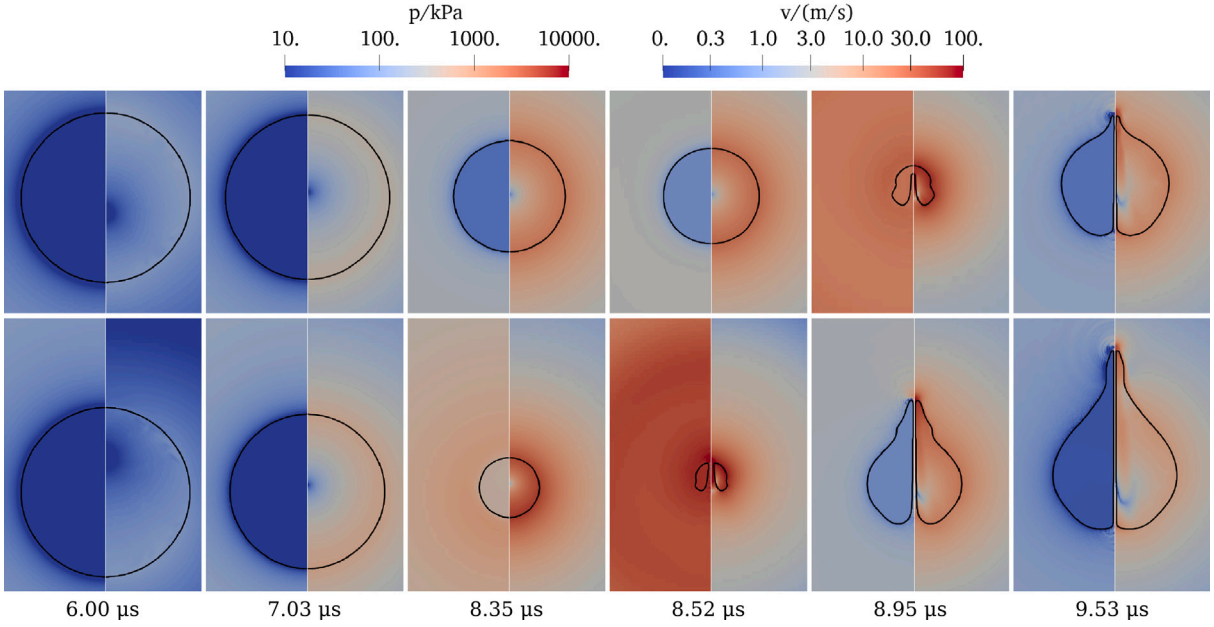

Fig. 4. Aligned jets in the case of two bubbles placed in a distance $D^* = 6.663$, with equilibrium bubble radii $R_E = 20\,\mu m$. The bubbles are excited with a single ultrasonic pulse with frequency $f = 100\,kHz$ and amplitude $p_A = 150\,kPa$. The top and bottom rows depict the top and bottom bubbles, respectively. The left and right side of each snapshot is colored according to the pressure and velocity magnitude, respectively.

of collapse (the point with zero velocity) is displaced upward from the geometric center of the bubble. The displacement of the velocity center is demonstrated in the Appendix in Fig. B.17. This results in a larger interface velocity in the bottom of the bubble, as this interface is farther away from the velocity center. Finally, as depicted in Fig. 4, the bottom bubble jets at 8.52 µs, while the top bubble jets at 8.95 µs. This time difference results from the combined effects of the ultrasonic pulse reaching the top bubble later (the time delay being $\Delta t = D/c = 0.36\,\mu s$) and the lower pressure difference experienced by the top bubble. The maximum jet velocities are 281 m/s and 165 m/s for the bottom and top bubbles, respectively.

3.3. Suppressing the jet formation

Jet formation of the top bubble can be suppressed above the threshold of opposing jets and below the threshold of aligned jets. In this case, the bottom bubble jets; however, the top bubble becomes more shape stable and collapses almost spherically, such a scenario is illustrated in Fig. 5. The bottom bubble reaches its minimum size and jets at 8.53 µs. The jetting and the subsequent shape of the bottom bubble is remarkably similar to those shown in Fig. 4, where the parameters are identical except for the distance between the bubbles.

The acoustic field around the top bubble is significantly influenced by the bottom bubble. Further analysis reveals that the mean pressure difference across the top bubble is −0.56 kPa throughout the collapse (compared to the 6.38 kPa experienced by the jetting bottom bubble), resulting in an almost spherical collapse without jetting at 8.91 µs, with only minor surface deformations. The bubble then expands spherically.

Fig. 6 examines the pressure and velocity fields around the top bubble during collapse for three cases with different D^* values, providing insights into the conditions that lead to jet suppression. In the case of $D^* = 1.287$ (Fig. 6a), the pressure around the top bubble loses its spherical symmetry early in the collapse process (visible at 8.00 µs). This asymmetry results in noticeable deformation. Ultimately,

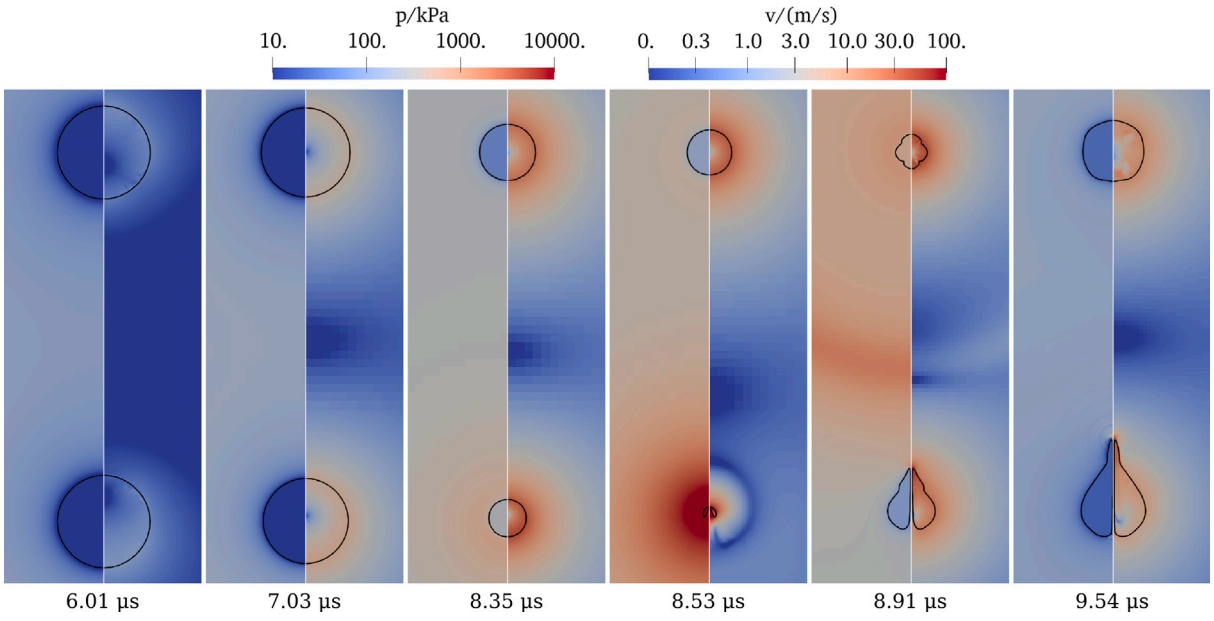

Fig. 5. Suppression of a bubble jet in the case of two bubbles placed in a distance $D^* = 3.937$, with equilibrium bubble radii $R_E = 20\,\mu m$. The bubbles are excited with a single ultrasonic pulse with frequency $f = 100\,kHz$ and amplitude $p_A = 150\,kPa$. The left and right side of each snapshot is colored according to the pressure and velocity magnitude, respectively.

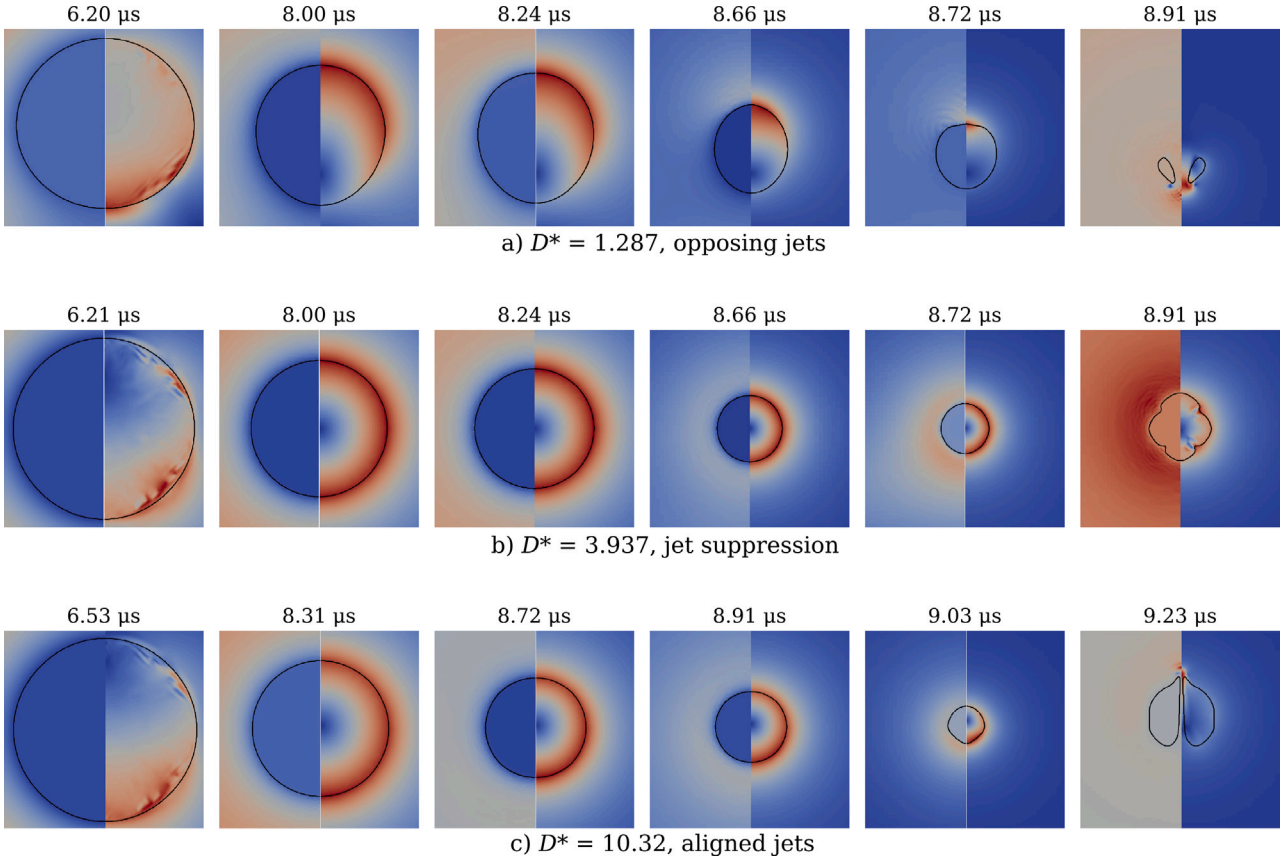

Fig. 6. Pressure (left side of each image) and velocity magnitude (right side of each image) around the top bubble in 3 cases with various D^* values. The parameters are $R_E = 20\,\mu m$, $f = 100\,kHz$ and $p_A = 150\,kPa$. The colorbar is rescaled in each time step to highlight the small differences in the fields.

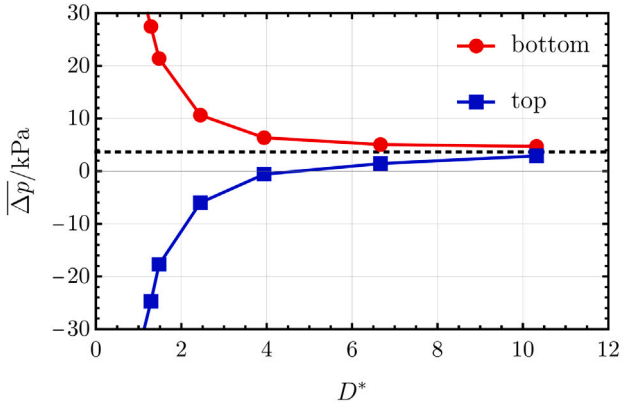

Fig. 7. Pressure difference across the top and bottom bubbles as a function of dimensionless distance D^* with parameters $R_E = 20\,\mu\text{m}$, $f = 100\,\text{kHz}$ and $p_A = 150\,\text{kPa}$. The dashed black line illustrates the value for a single bubble, that is $D^* \to \infty$.

the top bubble jets downward at the end of its collapse at 8.91 µs. In contrast, for $D^* = 10.32$ the top bubble remains nearly spherical until the final stages of collapse at 9.03 µs. However, the pressure and velocity fields around the bubble exhibit slight deviations from spherical symmetry, as observed at 8.72 µs and 8.91 µs. Jet suppression occurs due to the spherical symmetry of the pressure and velocity fields around the bubble throughout its collapse, as observed in Fig. 6b. Throughout the collapse, the pressure remains highly uniform around the bubble, leading to jet suppression. Although minor disturbances persist, resulting in slight non-sphericity visible in the bubble at 8.91 µs.

To quantitatively compare the three cases from above we define the mean pressure difference during collapse. The mean pressure difference is calculated by averaging the pressure difference across all time steps during which the bubble radius is decreasing. Fig. 7 illustrates the mean pressure difference across both bubbles as a function of the dimensionless distance D^* between them. The dashed black line in the figure represents the pressure difference experienced by a single bubble subjected to an ultrasonic pulse with the same parameters. In this case, the mean pressure difference during collapse is $\overline{\Delta p} = 3.7\,\text{kPa}$, which results from the shielding effect of the bubble — specifically, the pressure above the bubble is lower during collapse. As the distance between the bubbles increases, the mean pressure difference for both the top and bottom bubbles approaches the value for a single bubble. When the bubbles are close together ($D^* \leq 2$), the pressure between them drops significantly due to acoustic field shielding. This results in increasingly large pressure differences as D^* decreases. As shown in Fig. 7, there exists a region around $D^* \approx 4$ where the mean pressure difference across the top bubble during collapse is approximately zero. This corresponds to the case of jet suppression, as demonstrated in Figs. 5 and 6b.

Jet suppression is advantageous as it leads to an increased compression ratio within the top bubble. Fig. 8 illustrates the radius, pressure, and shape of the top bubble during collapse for different cases. The first column depicts the collapse of a single bubble with enforced spherical symmetry in ALPACA, where the internal pressure reaches $p_B = 99\,\text{MPa}$. In contrast, the pressure inside the bottom bubble is significantly lower, measuring 40 MPa for $D^* = 3.937$ and 9 MPa for $D^* = 1.287$. For the top bubble, the internal pressure reaches 69 MPa in the case of jet suppression ($D^* = 3.937$), whereas without jet suppression ($D^* = 1.287$), the pressure only reaches 30 MPa. These results demonstrate that jet suppression facilitates higher energy focusing within the bubble. Specifically, the conditions for spherical collapse in a single bubble can be approached when a bubble collapses without jetting.

3.4. Mesh independence study and validation

The convergence of the simulations is demonstrated for selected cases, as shown in Table 1. In case #1, jet suppression is observed in the top bubble, while the bottom bubble jets. In case #2, the top bubble collapses with small spherical distortion, and the bottom bubble is near the edge of the jet suppression domain. Cases #3 and #4 illustrate the phenomena of opposing and aligned bubble jets, respectively. For each case, at least three different mesh resolutions are applied. An initial mesh of 32×128 is adaptively refined using the multiresolution algorithm in ALPACA. The adaptive refinement in ALPACA always resolves interfaces with minimal sized cells. The number of adaptive mesh refinements (i.e., the maximum number of multiresolution levels) is provided in Table 1. The mesh resolution can be defined based on the proportion of the bubble diameter and the minimal cell size,

$$D_{\text{cell}} = \frac{2R_E}{a_{\min}}, \tag{13}$$

where the minimum cell size $a_{\min}$ is given by

$$a_{\min} = \frac{2\lambda}{128 \cdot 2^{l_{\max}}}. \tag{14}$$

Since the multiresolution algorithm allows for resolution jumps inside the bubble, D_{cell} does not necessarily equal the actual number of cells along the bubble diameter. Nonetheless, D_{cell} serves as a useful metric to describe the mesh resolution, as the bubble interface (where most numerical errors are generated) is always resolved with the smallest cells.

The simulation results for the bubble radius are also compared against the solution of the coupled Keller-Miksis equation. The Keller-Miksis equation describes the radius $R(t)$ of a spherical bubble in a varying pressure field, it considers the viscosity and the surface tension [56]. Furthermore, the incompressible pressure emission of the bubbles can be considered with finite propagation speed c_L based on Haghi and Kolios [57]. Due to the finite propagation speed, the pressure emitted from a bubble reaches the other bubble $\tau = D/c_L$ later. The coupled Keller-Miksis equation for a bubble pair with incompressible pressure emission reads:

$$\left(1 - \frac{\dot{R}_i}{c_L}\right) R_i \ddot{R}_i + \left(1 - \frac{\dot{R}_i}{3c_L}\right) \frac{3}{2} \dot{R}_i^2 = \left(1 + \frac{\dot{R}_i}{c_L} + \frac{R_i}{c_L} \frac{\mathrm{d}}{\mathrm{d}t}\right) \frac{p_{L,i}(R_i, t) - p_{\infty,i}(t)}{\rho_L} - \frac{1}{D} \sum_{j=1, j\neq i}^{2} \left(2\dot{R}_j(t-\tau) R_j(t-\tau) + R_j(t-\tau)^2 \ddot{R}_j(t-\tau)\right) \quad \text{with} \quad i = 1, 2, \tag{15}$$

where ρ_L is the liquid density and $p_{\infty,i}(t)$ is the acoustic excitation experienced by the ith bubble:

$$p_{\infty,i}(t) = p_0 - \begin{cases} p_A \sin\left(2\pi f (t - y_i/c_L)\right) & \text{if} \quad 0 < t - y_i/c_L < T \\ 0 & \text{else} \end{cases}, \tag{16}$$

with $y_1 = 0$ and $y_2 = D$. The liquid pressure at the bubble interface is given as

$$p_{L,i}(R_i, t) = p_{G,i}(t) - 4\mu_L \frac{\dot{R}_i(t)}{R_i(t)} - \frac{2\sigma}{R_i(t)}, \tag{17}$$

where σ is the coefficient of surface tension and μ_L is the viscosity of the liquid. The vapor pressure is neglected to facilitate complete agreement with the ALPACA simulations. The gas pressure inside the bubble is given as

$$p_{G,i}(t) = \left(\frac{2\sigma}{R_{E,i}} + p_0\right) \left(\frac{R_{E,i}}{R_i(t)}\right)^{3n_G}, \tag{18}$$

where $R_{E,i}$ is the equilibrium bubble radius. Eq. (15) is a delay differential equation, that was solved numerically using Wolfram Mathematica.

Fig. 9 illustrates the equivalent bubble radius of the top bubble in each case with various mesh resolutions (continuous lines). The

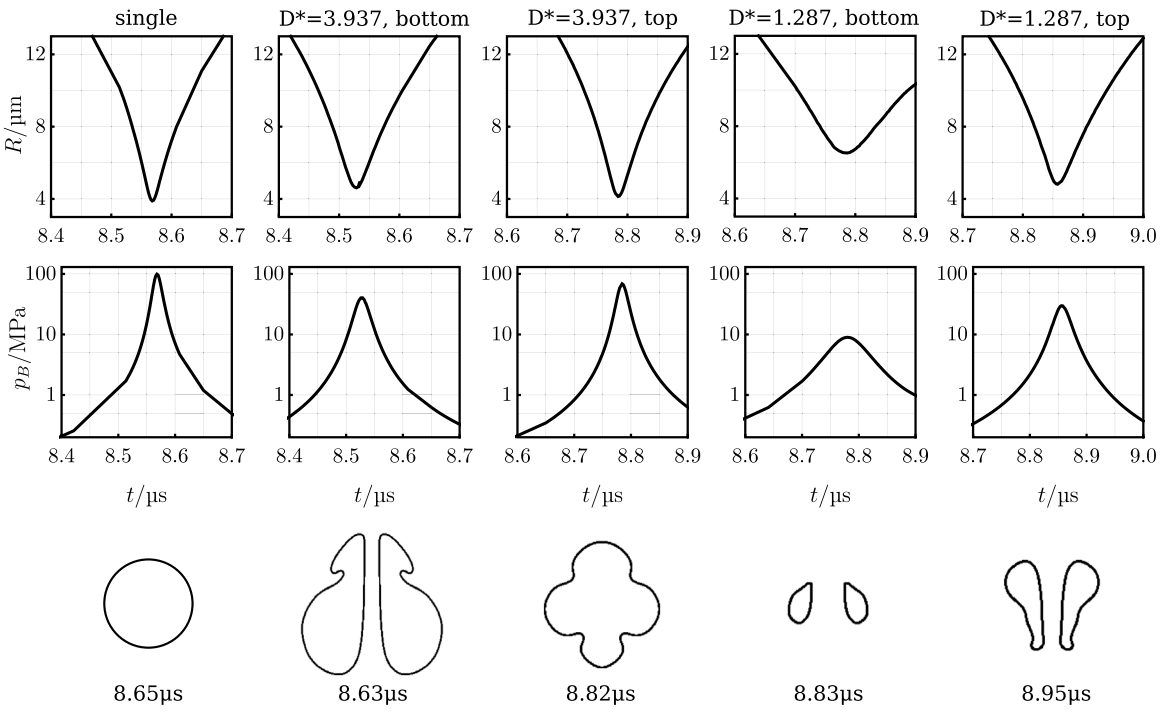

Fig. 8. Radius (top row), pressure (middle row) and shape of the bubble at a specified time step (bottom row) during collapse for bubbles with size $R_E = 20\,\mu m$. The bubbles are excited with a single pulse with $f = 100\,kHz$ and $p_A = 1.5\,bar$. The first column shows the collapse of a single bubble in spherical symmetry in ALPACA, further columns show the top and bottom bubble in axisymmetric bubble pair simulations.

Table 1
Parameters for mesh independence studies. The acoustic pressure amplitude is $p_A = 150\,kPa$ in each case.

#	Frequency f	Equilibrium radii R_E	Distance D	Phenomena	Levels l_{max}	Resolution D_{cell}
1	100 kHz	20 µm	320 µm	Jet suppression	8	43.8
					9	87.6
					10	175.2
					11	350.5
2	100 kHz	40 µm	380 µm	Jet suppression	8	87.6
					9	175.2
					10	350.5
					11	700.9
3	100 kHz	40 µm	180 µm	Opposing jets	8	87.6
					9	175.2
					10	350.5
					11	700.9
4	50 kHz	40 µm	160 µm	Aligned jets	9	87.6
					10	175.2
					11	350.5

ALPACA simulation results are compared against the coupled Keller-Miksis equation given in Eq. (15) (dashed black line). The equivalent radius is calculated from the bubble volume as

$$R = \sqrt[3]{\frac{3}{4\pi} V_B}. \tag{19}$$

The first expansion-collapse cycle is accurately resolved in each case in Fig. 9, independent of the applied mesh resolution, and the solution of the Keller-Miksis equation is reproduced. Major errors occur only after the first collapse. Fig. 9(a) demonstrates clear convergence with increasing resolution after the first collapse in case #1. A refinement level of $l_{max} = 10$ (corresponding to $D_{cell} = 175.2$) already provides accurate results for the bubble radius. In cases #2 and #3, the results are converged even at $l_{max} = 8$ ($D_{cell} = 87.6$), while in case #4, convergence is achieved at $l_{max} = 10$ (corresponding to $D_{cell} = 175.2$).

The convergence of the bubble shape is shown in Fig. 10 for case #1 at two time steps. The first row in panel Fig. 10a depicts the top bubble at 8.74 µs with increasing resolution from left to right, while the second row shows the bottom bubble at the same time instance. A clear convergence of the bubble shape is observed, confirming that the jet suppression of the top bubble is independent of mesh resolution. The bottom bubble jets similarly for $l_{max} \geq 10$ ($D_{cell} \geq 175.2$). Qualitative comparisons of the bubble shape, surrounding pressure, and velocity fields for each resolution are provided as videos in the supplementary material for each case listed in Table 1.

Based on the convergence studies, a mesh resolution of $D_{cell} = 175.2$ is sufficient to accurately simulate large bubble collapses, bubble

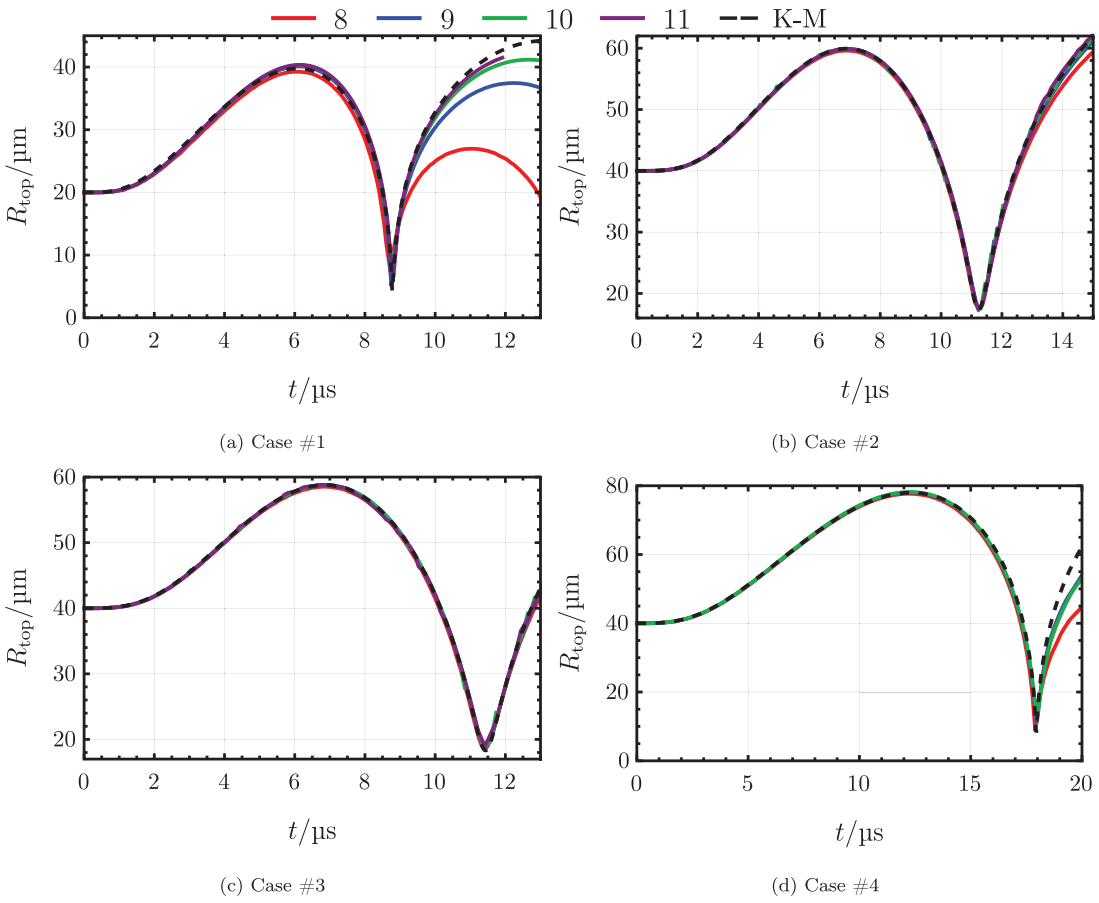

Fig. 9. Equivalent radius of the top bubble in the four convergence studies. The different colors represent the bubble radius at various mesh resolutions, as indicated by the maximum number of refinements, l_{max}, in the legend at the top. The solution of the Keller-Miksis equation (Eq. (15)) is indicated with a dashed black line.

jetting, and jet suppression. Further increasing the resolution does not yield additional relevant details for this study. This resolution also provides accurate bubble radii across all cases. Consequently, the mesh resolution was set to achieve $D_{\text{cell}} = 175.2$ for the remainder of this study. Further validation of the ALPACA code for non-spherical bubble oscillations and multiphase test cases can be found in other work of the authors [58]. The ALPACA solver was also validated for bubble jetting induced by shocks by Hoppe et al. [37], and for bubble jetting near solid surfaces by Bußmann et al. [49].

4. Domain of jet suppression

Bubbles in close proximity jet towards each other, whereas at greater separation distances, they exhibit aligned jets. In this section, the domain of jet suppression is defined as the range of separation between the domains of opposing and aligned jets. In the domain of jet suppression the jet formation in the top bubble is suppressed. The domain of jet suppression is analyzed as a function of the bubble radii and the excitation frequency of the ultrasonic pulse. To examine the effect of those parameters, 101 ALPACA simulations were carried out, the simulations lasted until (at least) the first collapse of both bubbles. The parameters for each simulation, as well as the observed phenomenon is detailed in the Appendix in Tables D.3, D.4, D.5 and D.6.

The jet suppression domain for each series of simulation with given equilibrium bubble radius R_E, excitation frequency f and pressure amplitude p_A is given in Table 2. To generalize the findings about the jet suppression domain we define the compression ratio as

$$\gamma = \frac{R_{\text{max}}}{R_{\text{min}}}, \tag{20}$$

and the dimensionless collapse time as

$$\tau_{\text{collapse}} = \frac{t_{\text{collapse}}}{T}, \tag{21}$$

where t_{collapse} is the time of the first bubble collapse. The compression ratio γ and the dimensionless collapse time τ_{collapse} is assigned for each series of simulation (with same bubble size, pressure amplitude, excitation frequency) for the case with $D^* \approx 4$. It should be noted that for bubbles closer to each other the compression ratio decreases, and for bubbles farther apart the compression ratio increases, the variation in γ is within 10%. Table 2 also depicts the lower and upper limit of jet suppression (D^*_{lower} and D^*_{upper}). The limits are determined by taking the mean value of D^* for the closest case above and below the limit. The error is based on the difference between the case closest above and below the limit.

4.1. Effect of frequency

Fig. 11 illustrates the jet suppression domain of the top bubble in terms of D^* in a bubble pair with radii $R_E = 40\,\mu\text{m}$. It is plotted as a function of the excitation frequency on a logarithmic scale, see the green shaded area. Red squares mark the parameters where aligned jets were observed, while red circles indicate parameters with opposing jets. Green circles denote cases where both bubbles underwent collapse without jet formation, whereas green squares represent the cases where the jet formation was suppressed in the top bubble, but not in the bottom bubble (this is called jet suppression in the top bubble). The shaded green background of the jet suppression domain is derived through interpolation of the results to the whole plane.

Table 2
The jet suppression domain of the top bubble as a function of compression ratio γ and dimensionless collapse time τ_{collapse} for various cases with different excitation frequency f, equilibrium bubble radius R_E and pressure amplitude p_A. The last two columns show the lower limit of jet suppression (D^*_{lower}) and the upper limit of jet suppression (D^*_{upper}).

#	γ	τ_{collapse}	f	R_E	p_A	D^*_{lower}	D^*_{upper}
1	1.573	1.685	100 kHz	80 μm	1.50 bar	0	∞
2	3.330	1.084	100 kHz	40 μm	1.50 bar	2.05 ± 0.06	∞
3	5.532	0.951	72 kHz	40 μm	1.50 bar	2.64 ± 0.29	11.5 ± 2.90
4	6.908	1.132	100 kHz	40 μm	2.79 bar	3.08 ± 0.93	7.02 ± 3.01
5	8.868	0.852	100 kHz	20 μm	1.50 bar	3.19 ± 0.75	5.30 ± 1.36
6	9.261	0.858	50 kHz	40 μm	1.50 bar	2.97 ± 0.48	6.11 ± 0.72
7	10.393	1.421	200 kHz	30 μm	7.60 bar	4.47 ± 0.15	5.51 ± 0.41
8	13.121	1.037	72.6 kHz	40 μm	2.79 bar	3.80 ± 0.20	4.62 ± 0.22
9	13.125	0.809	38.4 kHz	40 μm	1.50 bar	3.56 ± 0.15	4.42 ± 0.40
10	13.128	1.204	100 kHz	40 μm	4.59 bar	4.15 ± 0.15	5.48 ± 0.26
11	16.489	0.784	32 kHz	40 μm	1.50 bar	3.33 ± 0.19	3.91 ± 0.19
12	28.852	0.701	20 kHz	40 μm	1.50 bar	3.49 ± 0.18	3.85 ± 0.18

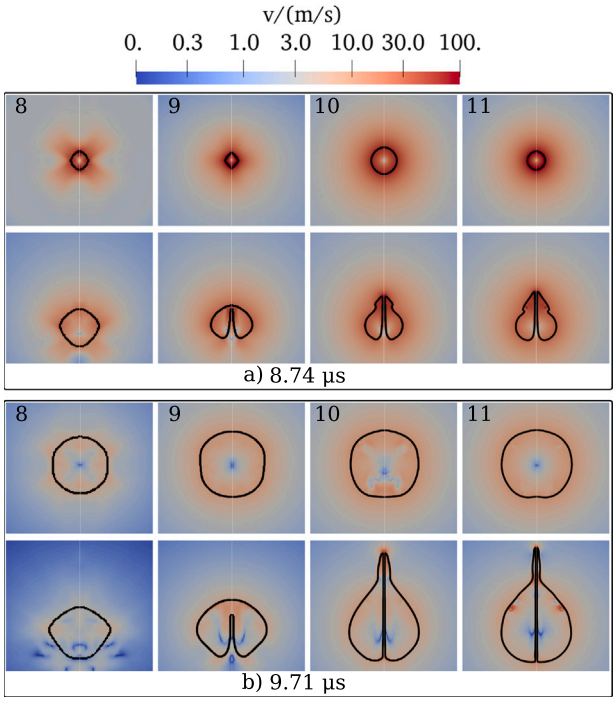

Fig. 10. Velocity field in convergence study #1 in two time steps with 4 mesh resolutions. The top row depicts the top bubble, while the bottom row depicts the bottom one for both steps. The columns correspond to simulation results with different mesh resolutions, with the numbers (8–11) indicating the number of adaptive mesh refinements l_{max}.

At $f = 100$ kHz frequency, the bubble expansion and collapse are less pronounced, with the compression ratio reaching only $\gamma = 3.33$. Due to the weaker collapse compared to lower frequencies, aligned bubble jets do not occur for distant bubbles, and both bubbles collapse spherically for $D^* > 4$. For closely spaced bubbles with $D^* < 2$, opposing bubble jets form. In the intermediate range, $2 < D^* < 4$, the jetting in the top bubble is suppressed, but for the bottom bubble a liquid jet still forms.

When the frequency is reduced to $f = 50$ kHz, the compression ratio increases to $\gamma = 9.26$ and distant bubbles with $D^* > 6$ produce aligned jets. The top bubble stabilizes approximately in the range $3 < D^* < 6$. As the frequency decreases further, the compression ratio increases, and the bubble collapse becomes increasingly violent. A shrinking jet suppression region is also observed: for $f = 32$ kHz, the top bubble stabilizes within $3.5 < D^* < 4.5$, while for $f = 20$ kHz, stable collapse occurs only in the simulation with $D^* = 3.674$. The results indicate that although bubbles at higher frequencies can be stabilized over a much wider range, their compression ratio is significantly smaller, making them less effective for sonochemistry. Jet suppression with large compression ratios at low frequencies is also possible, but it occurs only within a narrow region. From Fig. 11, it can also be obtained that the upper limit of jet suppression (separating jet suppression from aligned jets), as well as the lower limit (separating jet suppression from opposing jets) converges to $D^* \approx 3.67$ as the frequency is reduced.

4.2. Effect of bubble size

Similarly, the jet suppression domain is plotted for a case with constant frequency ($f = 100$ kHz) in Fig. 12. For $R_E = 20$ μm, a jet suppression domain of approximately $3 < D^* < 5$ is observed. For larger bubbles, the jet suppression domain increases, and for $R_E = 40$ μm, only opposing jets occur for $D^* < 2$, with no aligned jets observed. For bubbles with $R_E = 80$ μm, jetting was not observed at all; however, significant flattening of the facing bubble surfaces was noted during expansion for $D^* < 1$.

It should be noted that the compression ratio ($R_{\text{max}}/R_{\text{min}}$) decreases as the bubble size increases. For bubble sizes of $R_E = 20$ μm, 40 μm and 80 μm, the compression ratios are $\gamma = 8.89, 3.33$ and 1.57, respectively. This indicates that larger bubbles can be stabilized over a wider domain; however, their collapse is significantly weaker. Nonetheless, jet suppression is achievable for smaller bubbles as well, as demonstrated here for $R_E = 20$ μm. Similarly, as in the case before, the upper and lower limit of jet suppression seems to converge around $D^* \approx 4$.

4.3. Generalization with the compression ratio

As previously observed, the domain of jet suppression shrinks as the compression ratio increases. Additionally, it was noted that the jet suppression domain shifts to larger D^* values as the collapse time increases (see cases #8 – #10 in Table 2). The pressure gradient caused by acoustic excitation affects the bubbles only during the pulse, i.e., for $t < T$, where T is the period of excitation. If the collapse time exceeds the pulse duration, the influence of acoustic excitation diminishes. Consequently, the pressure field around the bubbles is increasingly dominated by bubble-bubble interactions. As a result, bubbles must be farther apart for the acoustic excitation to counteract the bubble-bubble interactions, shifting the stabilization domain towards larger D^* values.

The jet suppression domain as a function of the compression ratio (γ) is shown in Fig. 13 for cases where the collapse time satisfies $\tau_{\text{collapse}} < 0.9$ or the compression ratio is $\gamma < 8$. In these cases, jet suppression is clearly distinguishable from cases with aligned and opposing jets. For cases with a high compression ratio and a late collapse time ($\tau_{\text{collapse}} > 0.9$), this figure is no longer valid, as the stabilization domain shifts to larger D^* values. Based on Fig. 13, it can be concluded that for high compression ratios, the jet suppression domain converges around $D^* \approx 3.67$, provided that $\tau_{\text{collapse}} < 0.9$.

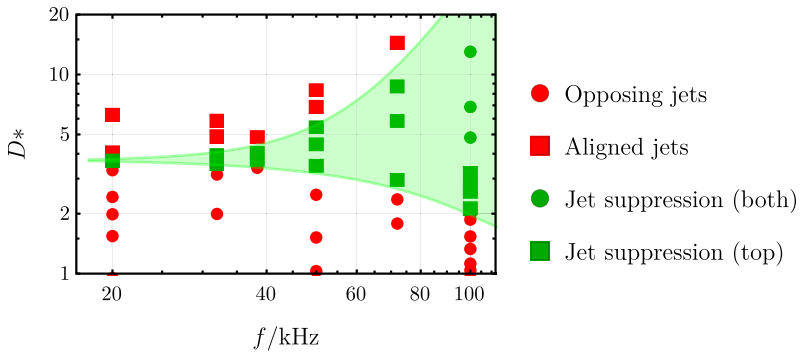

Fig. 11. Jet suppression of the top bubble in a bubble pair with $R_E = 40\,\mu m$ equilibrium radii as a function of excitation frequency f. The bubbles are excited with a traveling acoustic wave of amplitude $p_A = 150\,kPa$. The green background shows the jet suppression domain based on the numerical simulations.

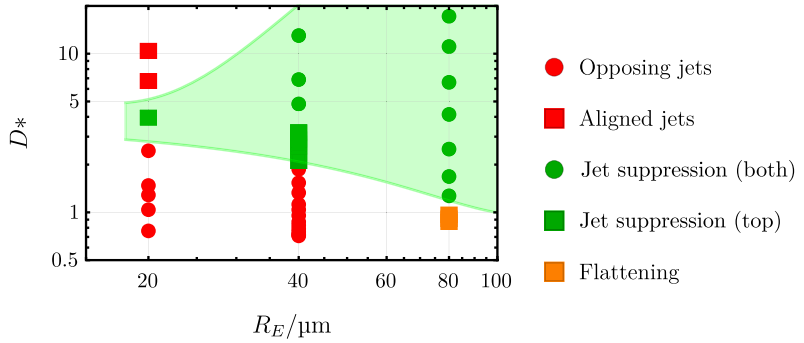

Fig. 12. Jet suppression domain of the top bubble in a bubble pair excited with $f = 100\,kHz$ and $p_A = 150\,kPa$ ultrasound as a function of equilibrium bubble radii R_E. The green background shows the jet suppression domain based on the numerical simulations.

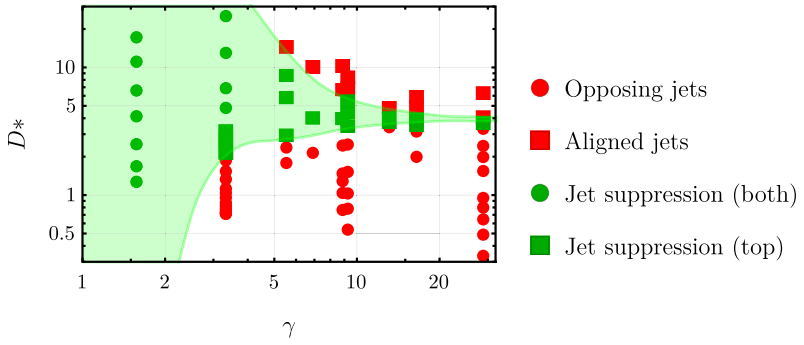

Fig. 13. Jet suppression of the top bubble in a bubble pair with various compression ratios. For each illustrated case with $\gamma > 8$, the dimensionless collapse time is $\tau_{collapse} < 0.9$. The green background shows the jet suppression domain based on the numerical simulations.

5. Conclusion

This paper presented a numerical investigation of bubble jet suppression in an oscillating bubble pair excited by an ultrasonic pulse. Jet suppression refers to the phenomenon where the bubble reached by the ultrasonic pulse later experiences reduced pressure gradients due to its specific placement, allowing it to collapse without jetting, while maintaining its spherical shape with minor distortion. This stabilized bubble collapse can be advantageous for applications focusing on chemical production inside the bubble, as the collapse is more focused and as bubble jets can dissipate a significant amount of energy. This was demonstrated for a specific case, for which the pressure inside a spherically collapsing bubble reached 99 MPa. In case of jet suppression 69.7% of this pressure was achieved in the top bubble of a bubble pair. Without jet suppression only 40.4% was reached. Jet suppression

consistently occurred over a range of parameters (frequency and bubble radius) when the distance between the bubbles was appropriately chosen. Convergence studies confirmed that jet suppression is independent of the numerical mesh, provided a sufficiently high resolution is used. To ensure accuracy, all simulations were conducted with a resolution of $D_{\text{cell}} = 175.2$, where $D_{\text{cell}} = 2R_E/a_{\min}$ represents the ratio of the equilibrium bubble diameter ($2R_E$) to the minimum cell size ($a_{\min}$) in the initial configuration.

The main findings of our work indicate that the domain of jet suppression narrows with increasing bubble compression and shifts to larger D^* values with increasing collapse time. This was demonstrated by decreasing the excitation frequency or bubble size, which results in larger compression ratios. These results suggest that while jet suppression in bubble pairs with large compression ratios is achievable, it becomes more sensitive to the separation distance. In the future more research is needed to examine the exact relation between the collapse time and upward shift in the jet suppression domain.

Jet suppression could potentially be utilized in sonochemical reactors to ensure the sphericity of bubbles. In multi-bubble systems with more than two bubbles aligned along an axis, a specific distance could be chosen between each bubble to maintain sphericity and increase compression. However, due to the damping of the ultrasonic pulse, the distribution may not be equidistant. In conjunction with advanced control algorithms for the bubble position [59], structured bubble grids could be achieved in sonochemical reactors. Optimizing such structured bubble layouts for jet suppression could enhance the chemical output of reactors.

CRediT authorship contribution statement

Dániel Nagy: Writing – review & editing, Writing – original draft, Visualization, Validation, Software, Methodology, Investigation, Formal analysis, Data curation, Conceptualization. **Ferenc Hegedűs:** Writing – review & editing, Supervision, Resources, Project administration, Conceptualization.

Declaration of competing interest

The authors declare that they have no known competing financial interests or personal relationships that could have appeared to influence the work reported in this paper.

Acknowledgments

This research was supported by the EKÖP, Hungary funded by the National Research Development and Innovation Fund under grant number EKÖP-24-3-BME-84. Project no. TKP-6-6/PALY-2021 has been implemented with the support provided by the Ministry of Culture and Innovation of Hungary from the National Research, Development and Innovation Fund, financed under the TKP2021-NVA funding scheme. The authors acknowledge the financial support of the Hungarian National Research, Development and Innovation Office via NKFIH grant OTKA FK142376.

Appendix A. Realizability of the ideal ultrasonic pulse

Since generating the pulse shown in Fig. 2 requires infinite acceleration of the transducer, it cannot be perfectly replicated in experiments. This appendix demonstrates that a good approximation of the described pulse is sufficient to reproduce jet suppression. The ideal acoustic pulse used throughout the paper is shown as a function of time in Fig. A.14 (dashed black line). This ideal pulse can be approximated using various methods:

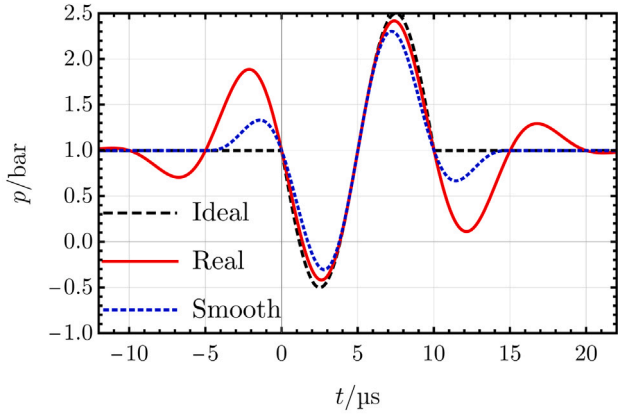

Fig. A.14. Approximation of the ideal pulse used in the paper with various methods.

1. State-of-the-art techniques allow for arbitrary waveform generation, enabling the creation of a smoothened version of the pressure pulse [60,61]. For example, Ohl et al. [24] investigated Gaussian pulses propagating through a bubbly fluid, generated by a modified medical lithotripter. The smoothened version of the ideal pulse is depicted in Fig. A.14. The initial difference should not significantly affect the dynamics, as it primarily influences the expansion of the bubble, not the collapse. Since bubble jetting is more dependent on the collapse phase, this modification should not alter the key findings.
2. Traditional piezo-transducers with a low transition time can reach the maximum amplitude quickly and have been used in many studies [62–64]. In this case, jet suppression could still occur, as during the first expansion-collapse cycle, bubbles with smaller radial oscillations experience only a reduced pressure amplitude, allowing them to remain spherical. This type of pulse is depicted in Fig. A.14 (continuous red line).

Fig. A.15 depicts the top bubble for the case of equilibrium bubble radii $R_E = 20\,\mu\text{m}$, excited by an ultrasonic pulse with $p_A = 1.5\,\text{bar}$ and $f = 100\,\text{kHz}$. The dimensionless distance between bubbles is $D^* = 3.937$. In Fig. A.15a, it can be observed that bubble jetting is also suppressed when the bubble is excited by a realistic pulse (as shown in Fig. A.14). For reference, Fig. A.15b shows the case where the bubble is excited by the ideal pulse. These results suggest that jet suppression can be successfully reproduced in experiments.

Appendix B. Collapse center of the bubble

This Appendix aim to demonstrate that bubbles experience a pressure difference during collapse (see Fig. B.16) that leads to the displacement of the velocity center. The pressure difference is defined as the difference in pressure above and below the bubble, that is $\Delta p = p_{\text{above}} - p_{\text{below}}$. The displacement of the velocity center (where $v = 0$) during expansion and collapse is demonstrated in Fig. B.17. As the velocity center is displaced during collapse, a bubble jet also forms.

Appendix C. Supplementary videos

The supplementary files contain videos of the 4 convergences studies introduced in Table 1. The 2 × 2 grid displays simulation results at increasing resolutions. Starting from the top left panel with the lowest resolution, the resolution doubles in the top right panel, doubles again in the bottom left panel, and reaches the highest resolution in the bottom right panel.

Appendix D. Parameters for each simulation

See Tables D.3–D.6

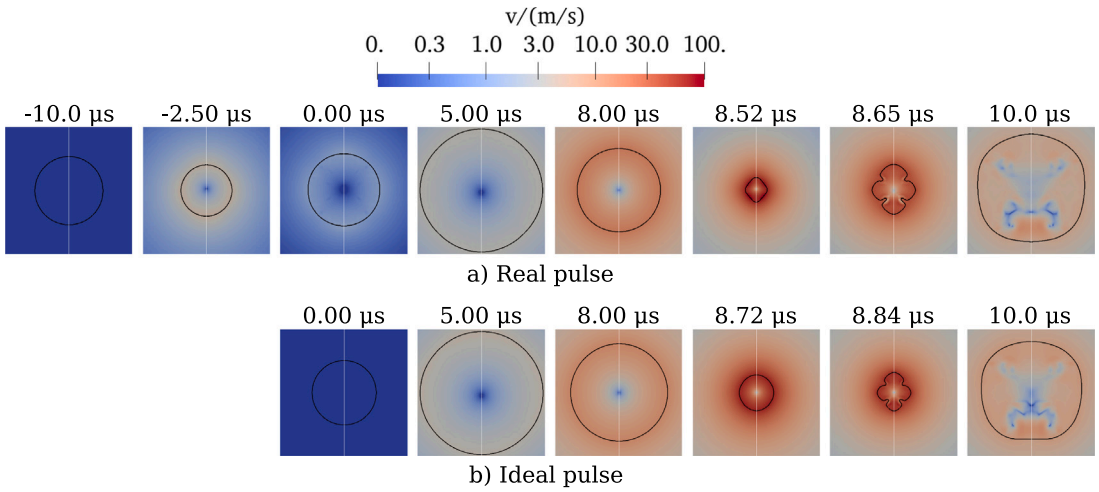

Fig. A.15. The top bubble in the case of a bubble pair with equilibrium radii $R_E = 20\,\mu\text{m}$ excited by an ultrasonic pulse with $p_A = 1.5\,\text{bar}$ and $f = 100\,\text{kHz}$.

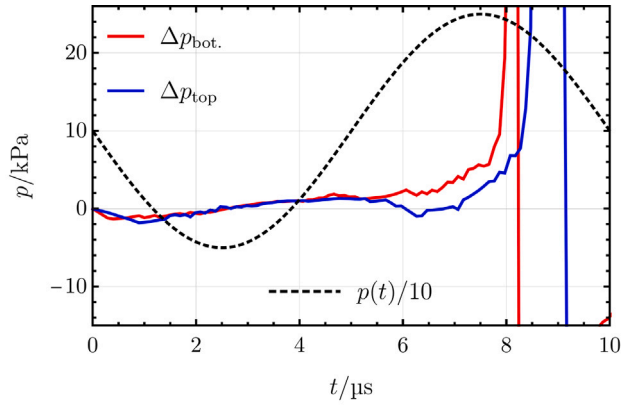

Fig. B.16. The pressure difference across the top and bottom bubbles in bubble pair excited with an ultrasonic pulse with parameters $D = 540\,\mu\text{m}$, $R_E = 20\,\mu\text{m}$, $f = 100\,\text{kHz}$ and $p_A = 150\,\text{kPa}$.

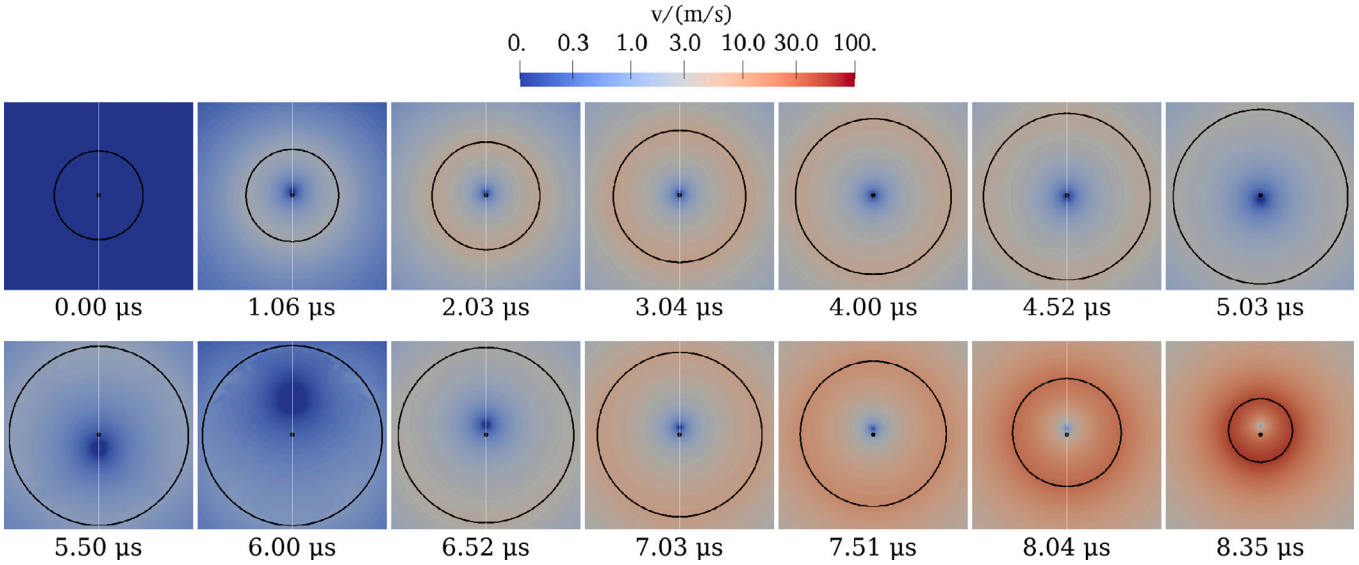

Fig. B.17. The bottom bubble of a bubble pair with parameters $D = 540\,\mu\text{m}$, $R_E = 20\,\mu\text{m}$, $f = 100\,\text{kHz}$ and $p_A = 150\,\text{kPa}$. Each snapshot is colored according to the velocity magnitude, the black dot depicts the bubble center.

Table D.3
Summary of all the simulations. (Part I).

$R_E/\mu m$	f/kHz	$D/\mu m$	D^*	$t_{jet}^{bot.}/\mu s$	$t_{jet}^{top}/\mu s$	comment
$p_A = 1.50\,bar$						
20	100	41	0.5339	–	–	Coalesce at $t = 2.63\,\mu s$
20	100	60	0.7643	8.81	8.93	opposing jets
20	100	80	1.0390	8.82	8.95	opposing jets
20	100	100	1.2868	8.83	8.95	opposing jets
20	100	120	1.4773	8.73	8.85	opposing jets
20	100	200	2.4445	8.62	8.86	opposing jets
20	100	320	3.9372	8.53	–	jet suppression
20	100	540	6.6626	8.52	8.97	aligned jet
20	100	840	10.3166	8.54	9.13	aligned jet
20	100	∞	∞	8.52	–	upward jet
40	100	81	0.7109	–	–	Coalesce at $t = 5.44\,\mu s$
40	100	82	0.7194	11.65	11.65	opposing jets
40	100	83	0.7280	11.65	11.65	opposing jets
40	100	86	0.7533	11.65	11.65	opposing jets
40	100	90	0.7872	11.64	11.64	opposing jets
40	100	95	0.8293	11.64	11.76	opposing jets
40	100	100	0.8717	11.63	11.76	opposing jets
40	100	110	0.9556	11.76	11.76	opposing jets
40	100	120	1.0392	11.74	11.74	opposing jets
40	100	130	1.1224	11.73	11.73	opposing jets
40	100	155	1.3300	11.71	11.84	opposing jets
40	100	180	1.5366	11.75	11.95	opposing jets
40	100	220	1.8668	12.06	12.84	opposing jets
40	100	235	1.9904	12.11	14.14	opposing jets
40	100	250	2.1136	12.44	–	jet suppression
40	100	305	2.5661	15.62	–	jet suppression
40	100	320	2.6894	19.21	–	jet suppression
40	100	340	2.8534	–	–	halting bottom jet
40	100	380	3.1816	–	–	halting bottom jet
40	100	580	4.8218	–	–	spherical collapse
40	100	830	6.8708	–	–	spherical collapse
40	100	1580	13.007	–	–	spherical collapse
40	100	3080	25.245	–	–	spherical collapse
40	100	∞	∞	–	–	spherical collapse

Table D.4
Summary of all the simulations. (Part II).

R_E/μm	f/kHz	D/μm	D^*	$t_{\text{jet}}^{\text{bot.}}$/μs	$t_{\text{jet}}^{\text{top}}$/μs	comment
$p_A = 1.50$ bar						
80	100	162	0.8651	–	–	Coalesce at $t = 11.14$ μs
80	100	170	0.9069	–	–	flattening
80	100	180	0.9590	–	–	flattening
80	100	240	1.2704	–	–	spherical collapse
80	100	320	1.6822	–	–	spherical collapse
80	100	480	2.5045	–	–	spherical collapse
80	100	800	4.1430	–	–	spherical collapse
80	100	1280	6.5992	–	–	spherical collapse
80	100	2160	11.093	–	–	spherical collapse
80	100	3360	17.222	–	–	spherical collapse
80	100	∞	∞	–	–	spherical collapse
40	50	81	0.5359	–	–	Coalesce at $t = 4.49$ μs
40	50	120	0.7820	17.69	17.82	opposing jets
40	50	160	1.0297	17.72	17.84	opposing jets
40	50	240	1.5188	17.53	17.77	opposing jets
40	50	400	2.4894	17.43	17.79	opposing jets
40	50	560	3.4567	17.43	–	jet suppression
40	50	720	4.4235	17.20	–	jet suppression
40	50	880	5.3925	17.12	–	jet suppression
40	50	1040	6.8368	17.12	18.12	aligned jet
40	50	1360	8.2840	17.13	18.12	aligned jet
40	50	∞	∞	17.13	–	upward jet
40	20	81	0.3343	–	–	Coalesce at $t = 7.70$ μs
40	20	120	0.4896	37.20	37.20	opposing jets
40	20	160	0.6453	37.09	37.09	opposing jets
40	20	240	0.9494	37.08	37.56	opposing jets
40	20	400	1.5437	37.03	37.62	opposing jets
40	20	520	1.9861	37.11	37.53	opposing jets
40	20	640	2.4326	36.71	37.52	opposing jets
40	20	880	3.3070	36.51	37.61	opposing jets
40	20	980	3.6736	36.51	–	jet suppression
40	20	1080	4.0398	36.62	37.53	aligned jet
40	20	1680	6.2364	36.65	37.53	aligned jet
40	20	∞	∞	36.60	–	upward jet

Table D.5
Summary of all the simulations. (Part III).

R_E/μm	f/kHz	D/μm	D^*	$t_{\text{jet}}^{\text{bot.}}$/μs	$t_{\text{jet}}^{\text{top}}$/μs	comment
$p_A = 1.50$ bar						
40	72	81	1.7842	–	–	opposing jets
40	72	120	2.3591	17.69	17.82	opposing jets
40	72	160	2.9325	17.72	17.84	jet suppression
40	72	240	5.7947	17.53	17.77	jet suppression
40	72	400	8.6512	17.43	17.79	jet suppression
40	72	560	14.356	17.43	–	aligned jet
40	72	∞	∞	17.43	–	upward jets
40	32	120	1.9935	24.78	25.49	opposing jets
40	32	160	3.1464	24.88	25.11	opposing jets
40	32	240	3.5299	24.72	–	jet suppression
40	32	400	3.9110	24.56	–	jet suppression
40	32	520	4.8695	24.59	25.53	aligned jet
40	32	640	5.8251	24.67	25.61	aligned jet
40	38.4	630	3.402	21.18	21.92	opposing jets
40	38.4	688	3.708	21.22	–	jet suppression
40	38.4	746	4.015	21.14	–	jet suppression
40	38.4	898	4.817	21.20	21.94	aligned jet
$p_A = 2.79$ bar						
40	100	320	2.142	11.58	11.87	opposing jets
40	100	610	4.009	11.42	–	jet suppression
40	100	1550	10.037	11.38	12.56	aligned jets
40	72	666	3.608	14.29	14.94	opposing jets
40	72	740	3.999	14.26	–	jet suppression
40	72	816	4.400	14.28	–	jet suppression
40	72	900	4.844	14.26	15.16	aligned jets

Table D.6
Summary of all the simulations. (Part IV).

R_E/μm	f/kHz	D/μm	D^*	$t_{\text{jet}}^{\text{bot.}}$/μs	$t_{\text{jet}}^{\text{top}}$/μs	comment
$p_A = 4.59$ bar						
40	100	760	3.995	12.02	12.71	opposing jets
40	100	820	4.303	12.00	–	jet suppression
40	100	1000	5.225	11.92	–	jet suppression
40	100	1100	5.738	11.93	12.96	aligned jets
$p_A = 7.60$ bar						
30	200	540	4.033	7.18	7.76	opposing jets
30	200	580	4.323	7.16	7.94	opposing jets
30	200	620	4.615	7.15	–	jet suppression
30	200	688	5.110	7.14	–	jet suppression
30	200	800	5.922	7.11	–	jet suppression
30	200	900	6.649	7.08	8.40	aligned jets

Appendix E. Supplementary data

Supplementary material related to this article can be found online at https://doi.org/10.1016/j.ultsonch.2025.107349.

References

[1] W. Lauterborn, H. Bolle, Experimental investigations of cavitation-bubble collapse in the neighbourhood of a solid boundary, J. Fluid Mech. 72 (2) (1975) 391–399.
[2] W. Lauterborn, C.-D. Ohl, Cavitation bubble dynamics, Ultrason. Sonochemistry 4 (2) (1997) 65–75.
[3] A. Vogel, W. Lauterborn, R. Timm, Optical and acoustic investigations of the dynamics of laser-produced cavitation bubbles near a solid boundary, J. Fluid Mech. 206 (1989) 299–338.
[4] M. Dular, O. Coutier-Delgosha, Numerical modelling of cavitation erosion, Internat. J. Numer. Methods Fluids 61 (12) (2009) 1388–1410.
[5] Y. Asakura, T. Nishida, T. Matsuoka, S. Koda, Effects of ultrasonic frequency and liquid height on sonochemical efficiency of large-scale sonochemical reactors, Ultrason. Sonochemistry 15 (3) (2008) 244–250.
[6] S. Merouani, H. Ferkous, O. Hamdaoui, Y. Rezgui, M. Guemini, A method for predicting the number of active bubbles in sonochemical reactors, Ultrason. Sonochemistry 22 (2015) 51–58.
[7] A. Thiemann, F. Holsteyns, C. Cairós, R. Mettin, Sonoluminescence and dynamics of cavitation bubble populations in sulfuric acid, Ultrason. Sonochemistry 34 (2017) 663–676.
[8] S. Sochard, A. Wilhelm, H. Delmas, Modelling of free radicals production in a collapsing gas-vapour bubble, Ultrason. Sonochemistry 4 (2) (1997) 77–84.
[9] S. Cho, S.H. Yun, Structure and optical properties of perovskite-embedded dual-phase microcrystals synthesized by sonochemistry, Commun. Chem. 3 (1) (2020) 1–7.
[10] F. Kubicsek, Á. Kozák, T. Turányi, I.G. Zsély, M. Papp, A. Al-Awamleh, F. Hegedûs, Ammonia production by microbubbles: A theoretical analysis of achievable energy intensity, Ultrason. Sonochemistry 106 (2024) 106876.
[11] A. Al-Awamleh, F. Hegedűs, Sono-hydrogen: a theoretical investigation of its energy intensity, Period. Polytech. Mech. Eng. 68 (3) (2024) 254–263.
[12] J. Mur, F. Reuter, V. Agrež, C.-D. Ohl, et al., Optic generation and perpetuation of acoustic bubble clusters, Ultrason. Sonochemistry 110 (2024) 107023.
[13] P. Adamou, E. Harkou, S. Hafeez, G. Manos, A. Villa, S. Al-Salem, A. Constantinou, N. Dimitratos, Recent progress on sonochemical production for the synthesis of efficient photocatalysts and the impact of reactor design, Ultrason. Sonochemistry (2023) 106610.
[14] K. Okitsu, F. Cavalieri, S.K. Bhangu, E. Colombo, M. Ashokkumar, Sonochemical Production of Nanomaterials, Springer, 2018.
[15] K. Qi, C. Zhuang, M. Zhang, P. Gholami, A. Khataee, Sonochemical synthesis of photocatalysts and their applications, J. Mater. Sci. Technol. 123 (2022) 243–256.
[16] M.H. Islam, O.S. Burheim, B.G. Pollet, Sonochemical and sonoelectrochemical production of hydrogen, Ultrason. Sonochemistry 51 (2019) 533–555.
[17] H. Xu, B.W. Zeiger, K.S. Suslick, Sonochemical synthesis of nanomaterials, Chem. Soc. Rev. 42 (7) (2013) 2555–2567.
[18] A. Zhang, S.-M. Li, P. Cui, S. Li, Y.-L. Liu, A unified theory for bubble dynamics, Phys. Fluids 35 (3) (2023).
[19] J. Yin, Y. Zhang, J. Zhu, Y. Zhang, S. Li, On the thermodynamic behaviors and interactions between bubble pairs: A numerical approach, Ultrason. Sonochemistry 70 (2021) 105297.
[20] J.A. Agha, K.M. Manmi, A. Dadvand, Dynamics of a bubble-pair between two parallel rigid walls, Ocean Eng. 301 (2024) 117401.
[21] J. Mur, A. Bußmann, T. Paula, S. Adami, N.A. Adams, C.-D. Ohl, et al., Microjet formation induced by the interaction of a spherical and toroidal cavitation bubble, Ultrason. Sonochemistry 112 (2025) 107185.
[22] J. Zhao, J. Wang, S. Cao, Dynamics of tandem bubble interaction near tissue, Phys. Fluids 36 (5) (2024).
[23] F. Yuan, G. Sankin, P. Zhong, Dynamics of tandem bubble interaction in a microfluidic channel, J. Acoust. Soc. Am. 130 (5) (2011) 3339–3346.
[24] S.-W. Ohl, J.M. Rosselló, D. Fuster, C.-D. Ohl, Finite amplitude wave propagation through bubbly fluids, Int. J. Multiph. Flow 176 (2024) 104826.
[25] Y. Shen, L. Zhang, Y. Wu, W. Chen, The role of the bubble–bubble interaction on radial pulsations of bubbles, Ultrason. Sonochemistry 73 (2021) 105535.
[26] Y. Zhang, K. Chen, Y. You, W. Ren, Interaction of two differently sized bubbles in a viscous liquid, Asia-Pac. J. Chem. Eng. 13 (3) (2018) e2192.
[27] B. Han, K. Köhler, K. Jungnickel, R. Mettin, W. Lauterborn, A. Vogel, Dynamics of laser-induced bubble pairs, J. Fluid Mech. 771 (2015) 706–742.
[28] P. Cui, Q. Wang, S. Wang, A. Zhang, Experimental study on interaction and coalescence of synchronized multiple bubbles, Phys. Fluids 28 (1) (2016).
[29] N. Bremond, M. Arora, S.M. Dammer, D. Lohse, Interaction of cavitation bubbles on a wall, Phys. Fluids 18 (12) (2006).
[30] Y.-H. Chen, L. I, Dynamics of impacting a bubble by another pulsed-laser-induced bubble: Jetting, fragmentation, and entanglement, Phys. Rev. E—Stat. Nonlinear, Soft Matter Phys. 77 (2) (2008) 026304.
[31] W. Liang, R. Chen, J. Zheng, X. Li, F. Lu, Interaction of two approximately equal-size bubbles produced by sparks in a free field, Phys. Fluids 33 (6) (2021).
[32] L.W. Chew, E. Klaseboer, S.-W. Ohl, B.C. Khoo, Interaction of two differently sized oscillating bubbles in a free field, Phys. Rev. E—Stat. Nonlinear, Soft Matter Phys. 84 (6) (2011) 066307.
[33] T. Hopfes, Z. Wang, M. Giglmaier, N.A. Adams, Collapse dynamics of bubble pairs in gelatinous fluids, Exp. Therm. Fluid Sci. 108 (2019) 104–114.
[34] B. Biller, N. Hoppe, S. Adami, N.A. Adams, Jetting mechanisms in bubble-pair interactions, Phys. Fluids 34 (7) (2022).
[35] J. Rosselló, W. Lauterborn, M. Koch, T. Wilken, T. Kurz, R. Mettin, Acoustically induced bubble jets, Phys. Fluids 30 (12) (2018).
[36] S.W. Fong, D. Adhikari, E. Klaseboer, B.C. Khoo, Interactions of multiple spark-generated bubbles with phase differences, Exp. Fluids 46 (2009) 705–724.
[37] N. Hoppe, J.M. Winter, S. Adami, N.A. Adams, ALPACA - a level-set based sharp-interface multiresolution solver for conservation laws, Comput. Phys. Comm. 272 (2022) 108246.
[38] N. Hoppe, S. Adami, N.A. Adams, A parallel modular computing environment for three-dimensional multiresolution simulations of compressible flows, Comput. Methods Appl. Mech. Engrg. 391 (2022) 114486.
[39] S. Cleve, M. Guédra, C. Mauger, C. Inserra, P. Blanc-Benon, Microstreaming induced by acoustically trapped, non-spherically oscillating microbubbles, J. Fluid Mech. 875 (2019) 597–621.
[40] M. Guédra, C. Inserra, Bubble shape oscillations of finite amplitude, J. Fluid Mech. 857 (2018) 681–703.
[41] C. Kalmár, K. Klapcsik, F. Hegedűs, Relationship between the radial dynamics and the chemical production of a harmonically driven spherical bubble, Ultrason. Sonochemistry 64 (2020) 104989.
[42] X.Y. Hu, B. Khoo, N.A. Adams, F. Huang, A conservative interface method for compressible flows, J. Comput. Phys. 219 (2) (2006) 553–578.
[43] G.-S. Jiang, D. Peng, Weighted ENO schemes for Hamilton–Jacobi equations, SIAM J. Sci. Comput. 21 (6) (2000) 2126–2143.
[44] S. Osher, R. Fedkiw, K. Piechor, Level set methods and dynamic implicit surfaces, Appl. Mech. Rev. 57 (3) (2004) B15.
[45] V. Bogdanov, F.S. Schranner, J.M. Winter, S. Adami, N.A. Adams, A level-set-based sharp-interface method for moving contact lines, J. Comput. Phys. 467 (2022) 111445.
[46] L. Fu, X.Y. Hu, N.A. Adams, A family of high-order targeted ENO schemes for compressible-fluid simulations, J. Comput. Phys. 305 (2016) 333–359.
[47] N. Fleischmann, S. Adami, N. Adams, Numerical symmetry-preserving techniques for low-dissipation shock-capturing schemes, Comput. Fluids 189 (2019) 94–107, http://dx.doi.org/10.1016/j.compfluid.2019.04.004.

[48] N. Fleischmann, S. Adami, X. Hu, N. Adams, A low dissipation method to cure the grid-aligned shock instability, J. Comput. Phys. 401 (2020) 109004, http://dx.doi.org/10.1016/j.jcp.2019.109004.
[49] A. Bußmann, F. Riahi, B. Gökce, S. Adami, S. Barcikowski, N.A. Adams, Investigation of cavitation bubble dynamics near a solid wall by high-resolution numerical simulation, Phys. Fluids 35 (1) (2023).
[50] Y. Fan, A. Bußmann, F. Reuter, H. Bao, S. Adami, J.M. Gordillo, N. Adams, C.-D. Ohl, Amplification of supersonic microjets by resonant inertial cavitation-bubble pair, Phys. Rev. Lett. 132 (10) (2024) 104004.
[51] S.J. Shaw, Translation and oscillation of a bubble under axisymmetric deformation, Phys. Fluids 18 (7) (2006) 072104.
[52] F.H. Harlow, A.A. Amsden, Fluid Dynamics. A LASL Monograph, Tech. Rep., Los Alamos National Lab.(LANL), Los Alamos, NM (United States), 1971.
[53] J.W. Kaiser, N. Hoppe, S. Adami, N.A. Adams, An adaptive local time-stepping scheme for multiresolution simulations of hyperbolic conservation laws, J. Comput. Phys. 4 (2019) 100038.
[54] M. Postema, P. Marmottant, C.T. Lancée, S. Hilgenfeldt, N. De Jong, Ultrasound-induced microbubble coalescence, Ultrasound Med. Biol. 30 (10) (2004) 1337–1344.
[55] M. Postema, A. Van Wamel, C.T. Lancée, N. De Jong, Ultrasound-induced encapsulated microbubble phenomena, Ultrasound Med. Biol. 30 (6) (2004) 827–840.
[56] J.B. Keller, M. Miksis, Bubble oscillations of large amplitude, J. Acoust. Soc. Am. 68 (2) (1980) 628–633.
[57] H. Haghi, M.C. Kolios, The role of primary and secondary delays in the effective resonance frequency of acoustically interacting microbubbles, Ultrason. Sonochemistry 86 (2022) 106033.
[58] D. Nagy, S. Adami, F. Hegedűs, Direct numerical simulation of spherical and non-spherical bubble dynamics using the ALPACA compressible multiphase flow solver, 2025, Preprint.
[59] K. Klapcsik, B. Gyires-Tóth, J.M. Rosselló, F. Hegedűs, Position control of an acoustic cavitation bubble by reinforcement learning, Ultrason. Sonochemistry 115 (2025) 107290.
[60] J. Wang, S. Ota, H. Edlbauer, B. Jadot, P.-A. Mortemousque, A. Richard, Y. Okazaki, S. Nakamura, A. Ludwig, A.D. Wieck, et al., Generation of a single-cycle acoustic pulse: a scalable solution for transport in single-electron circuits, Phys. Rev. X 12 (3) (2022) 031035.
[61] V. Augutis, D. Gailius, E. Vastakas, P. Kuzas, Evaluation of arbitrary waveform acoustic signal generation techniques in dispersive waveguides, J. Vibrotech. 17 (7) (2015) 4047–4056.
[62] M. Versluis, D.E. Goertz, P. Palanchon, I.L. Heitman, S.M. van Der Meer, B. Dollet, N. De Jong, D. Lohse, Microbubble shape oscillations excited through ultrasonic parametric driving, Phys. Rev. E—Stat. Nonlinear, Soft Matter Phys. 82 (2) (2010) 026321.
[63] M.L. Buddensiek, C.M. Krawczyk, N. Kukowski, O. Oncken, Performance of piezoelectric transducers in terms of amplitude and waveform, Geophysics 74 (2) (2009) T33–T45.
[64] Y. Lin, L. Lin, M. Cheng, L. Jin, L. Du, T. Han, L. Xu, A.C. Yu, P. Qin, Effect of acoustic parameters on the cavitation behavior of SonoVue microbubbles induced by pulsed ultrasound, Ultrason. Sonochemistry 35 (2017) 176–184.